THE JOURNAL OF PHYSICAL CHEMISTRY Letters

Letter

pubs.acs.org/JPCL

Inherent Simple Cubic Lattice Being Responsible for Ultrafast Solid-Phase Change of $Ge_2Sb_2Te_5$

Wen-Xiong Song,[†,‡] Zhi-Pan Liu,*[,†,‡] and Li-Min Liu[‡]

[†]Collaborative Innovation Center of Chemistry for Energy Material, Key Laboratory of Computational Physical Science (Ministry of Education), Shanghai Key Laboratory of Molecular Catalysis and Innovative Materials, Department of Chemistry, Fudan University, Shanghai 200433, China

[‡]Beijing Computational Science Research Center, Beijing 100193, China

Supporting Information

ABSTRACT: Crystallization of solid is generally slow in kinetics for atoms trapped in solids. Phase-change materials (PCMs) challenge current theory on its ultrafast reversible amorphous-to-crystal transition. Here by using the stochastic surface walking global optimization method, we establish the first global potential energy surface (PES) for $Ge_2Sb_2Te_5$. By analyzing all structures on the global PES, we show that an inherent structural pattern of simple cubic lattice is present universally in low-energy structures, either globally in a newly found metastable simple cubic crystal phase or locally in the amorphous structures. Our solid-to-solid reaction pathway sampling reveals that this simple cubic lattice plays a critical role in the rapid amorphous-to-crystal transition, which occurs via dynamic vacancy creation/annihilation, Martensitic-type {100} shearing, and diffusionless local relaxation. This knowledge from global PES allows the prediction of PCMs by linking the phase-change kinetics with the geometry of metastable phases.

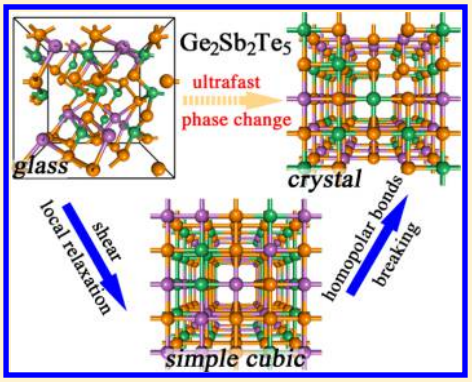

$Ge_2Sb_2Te_5$ (GST) phase-change material has great potentials for data recording in electrical devices.[1−4] It has a fast (∼ns) amorphous-to-crystal solid-phase transition that works at relatively low temperatures, that is, ∼150 °C, and exhibits the sharp switch of electronic/optical signals (e.g., ∼2 orders of magnitude in resistivity change) in the solid transition. While such rapid reversible solid transitions often imply a diffusionless transformation mechanism[2,5,6] typical in Martensitic transition between crystal phases[7] with a particular habit plane and a shape-memory effect, the long-range ordering in GST from amorphous to crystals is apparently not the case, where the amorphous phase of GST is known to have a large structural heterogeneity, as evident by the disordered vacancies and the presence of many new types of bonds (e.g., Ge−Ge and Te−Te).[1,8,9] This puzzle on the transition kinetics could be attributed to the lack of knowledge on intermediates between amorphous and crystal phases. New theoretical models are urgently called for to bridge the structure gap and resolve the atomic mechanism of amorphous-to-crystal transition.

The potential energy surface (PES) of GST is complex due to the presence of three elements.[10] To date, two stable classes of crystalline structures were observed for GST, hexagonal (***hex***) and rock-salt (***rs***) crystals, where ***rs*** is known as the product in the rapid amorphous-to-crystal transition. While the vacancy sites aggregate preferentially in ***hex*** and ***rs*** crystals, the amorphous phase tends to have randomly distributed cavities according to molecular dynamics (MD) simulations.[11,12] In addition, new bond types, for example, homopolar Ge−Ge, Sb−Sb, Te−Te, and Ge−Sb bonds, which are not present in the two stable crystalline phases, were observed in the amorphous phase[1,8] and also confirmed using reverse Monte Carlo to fit the experimental data.[13] It is thus expected that the amorphous-to-crystal transition involves atom displacement to annihilate the homopolar bonds and gradual vacancy ordering. This complex structural variation is apparently contradictory to the rapid reversible phase transition kinetics. Consequently, how the crystalline nucleus forms and grows in an amorphous matrix is still highly debated in the literature.[11,14,15]

Here we utilize novel Stochastic Surface Walking (SSW) global optimization to resolve the global PES of GST. The SSW method developed recently is designed to efficiently explore a complex PES via smooth surface walking along softened random directions.[7,16,17] This allows determination of the atomic structures for a huge amount of metastable structures on the global PES, including new metastable crystals and an amorphous phase, and statistical characterization of their common structural features. On the basis of the information from SSW trajectories,[18−20] we further identify low-energy reaction pathways linking amorphous structures to the ***rs*** phase, which helps to clarify the physical origin of the rapid amorphous-to-crystal transition.

Our investigation starts by exploring the PES of GST with SSW global optimization in the framework of van der Waals-corrected density functional theory (DFT) calculations[21] (see

Received: April 14, 2017
Accepted: May 23, 2017
Published: May 23, 2017

DOI: 10.1021/acs.jpclett.7b00913
J. Phys. Chem. Lett. 2017, 8, 2560−2564

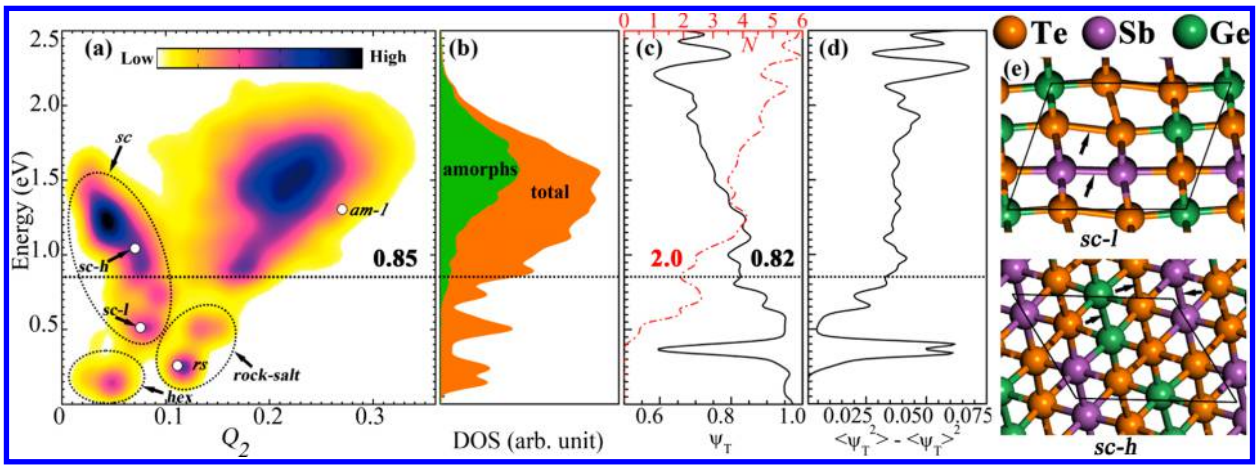

Figure 1. Global PES for GST minima from a SSW global search. (a) Contour plot for the density of states (DOS) of minima by plotting the energy of the state (minimum) against its Steinhardt order parameter Q_2 (degree l = 2). The energy E is with respect to the global minimum (the most stable hexagonal phase). Important structures are indicated in (a), including ***hex***: hexagonal; ***rs***: rock-salt; ***sc-l*** and ***sc-h***: two representative metastable crystalline phases that are free of vacancy. (b) One-dimensional DOS of minima. (c) Evolution for the translation order parameters (ψ_T) and the number of Te−Te bonds, N(Te−Te), averaged over all structures in a small energy window (E, $E+\delta E$), δE = 0.01 eV. (d): Evolution of the variance of the ψ_T parameter. The dotted lines in (a−d) at ∼0.85 eV/fu indicate the boundary separating amorphous from crystals. (e) Typical ***sc-l*** and ***sc-h*** structures.

the Supporting Information (SI) for all calculation details). The SSW search is carried out massively in parallel, starting from the known hexagonal crystal structure.[10] The search was found to rapidly escape from the initial configuration and explore the whole PES. We terminate the SSW search when a total of 13286 minima are collected that include a large variety of structures ranging from crystalline structures to amorphous structures. These minima on the PES are the inherent structures corresponding to the possible local structure patterns that occur when a material is cooled down rapidly.

To visualize the large data set, we constructed the global PES in Figure 1a using an $E \sim Q$ graph by plotting the total energy (E) per unit cell (9 atoms) of the minimum against a common structure fingerprint for the crystal, namely, the Steinhardt order parameter[22] with degree l = 2, Q_2. The corresponding density of states (DOS) is shown in Figure 1b. By inspecting carefully all of the structures, we are able to identify four major phase zones (see the figure), including three crystalline phases: (i) the hexagonal minima, (ii) the rock-salt minima, (iii) the metastable simple cubic structures (***sc***), and (iv) the amorphous structures.

hex *and* ***rs*** *Phases.* These two most stable phases have been studied extensively (e.g., refs 3, 23, and 24) and are not the main focus here. Consistent with the literature, we found that two phases contain vacancies often surrounded by Te atoms, either aggregated on a particular crystallography plane or distributed along a particular direction (see SI Figure S1 for ***hex***/***rs*** structures). The presence of vacancies is attributed to the requirement to break unfavorable Ge/Sb−Te antibondings.[3]

Simple Cubic Crystal Phase. The metastable ***sc*** phase has not been reported previously. It spans a large area in the global PES (Figure 1a). It is higher in energy (>0.3 eV/fu) compared to the most stable hexagonal crystal. The ***sc*** phase can be considered as a distorted rock-salt phase with all lattice sites being occupied by three elements randomly. Therefore, the ***sc*** phase has two important structural features: (i) homopolar bonds and (ii) lack of vacancies.

While there are a lot of minima (∼3500) in this area, we manage to distinguish two classes of structures with a high DOS, denoted as ***sc-l*** and ***sc-h*** (high energy). The representative structures of them are shown in Figure 1e. Obviously, all ***sc*** structures possess homopolar bonds, such as Te−Te, Sb−Sb, Ge−Ge, and Ge−Sb bonds, that are absent in the ***hex*** and ***rs*** phases. Due to the lack of vacancy, the ***sc*** phase is densely packed, for example, ∼263 Å^3 per formula unit (fu) for ***sc-l***, with its volume 3−7% smaller than the two more stable crystalline phases (271 for ***hex*** and 281 Å^3/fu for ***rs***). We note that the major structural difference between ***sc-l*** and ***sc-h*** is the number of homopolar bonds. As illustrated in Figure 1e, the typical ***sc-l*** has two Te−Te bonds and one Sb−Sb bond per unit cell, while the typical ***sc-h*** has four Te−Te, one Sb−Sb, and one Ge−Ge bonds per unit cell. This suggests that the homopolar bonds can destabilize significantly the material. Our electronic structure analyses show that the ***sc*** phase is metallic without a band gap (see Figure S2), suggesting a high conductivity similar to that of the other two crystalline phases.

It should be mentioned that the ***sc*** phase differs from the previously reported body-center cubic (bcc) GST phase found at high pressure (30 GPa),[25] although both phases are vacancy-free. We note that the bcc phase is unstable under ambient pressures; the structural relaxation of the bcc phase will lead to a high-energy amorphous structure from our DFT calculations.

Amorphous Phase. The amorphous structures occupy the largest area in the global PES and have a broad peak above ∼0.85 eV/fu in the DOS (Figure 1b). In order to distinguish the amorphous structures from (defected) crystalline structures, we have analyzed all structures based on two geometry parameters, the translational order parameter[26] ψ_T and the number of Te−Te homopolar bonds N(Te−Te) per fu. The ψ_T parameter in eq 1 is utilized to measure the deviation of the atom away from perfect lattice points

$$\psi_T = \frac{1}{N}\sum_{i=1}^{N}\cos(\vec{G}\cdot\vec{r}_i) \quad (1)$$

where $\vec{G}$ is the primary reciprocal lattice vector (simple cubic lattice utilized here), $\vec{r}_i$ is the position vector in real space, and

DOI: 10.1021/acs.jpclett.7b00913
J. Phys. Chem. Lett. 2017, 8, 2560−2564

N is the number of atoms in the supercell. $\psi_T = 1$ if all atoms are located at ideal lattice positions with deviation lowering the translational ordering. Apparently, for GST crystals, N(Te−Te) = 0 and ψ_T is close or equal to 1. In Figure 1c,d, we plot the change of ψ_T, N(Te−Te), and the variance of ψ_T (characterizing the structural heterogeneity) for all structures on the global PES.

Figure 1c,d shows that these structural parameters vary rapidly when the structures enter into the amorphous region because amorphous structures have a large number of homopolar bonds (large N(Te−Te)) and deviate increasingly away from the perfect simple cubic lattice (small ψ_T). From the figure, we can define roughly a boundary with E = 0.85 eV/fu, $\psi_T \approx 0.82$, and N(Te−Te) ≈ 2, which separates crystalline structures from amorphous ones. With this amorphous structure criteria, we screen out 4275 amorphous structures from the global PES data, and their DOS is shown as the filled green area in Figure 1b. It should be emphasized that the simple cubic lattice, although not present uniformly, remains as a key local structure pattern for low-energy amorphous structures, as reflected by ψ_T (~0.82). In Figures S3 and S4, we show the atom arrangement of 12 randomly selected low-energy amorphous structures, where the characteristic ⟨100⟩ square of simple cubic lattice is highlighted.

The amorphous structures have a wide distribution in volume, ranging from 260 to 310 Å^3/fu, suggesting a large heterogeneity in local structure. By counting the coordination number (CN) of the atom, we found that the volume expansion in amorphous structures is caused by an increase of low-coordinated atoms (all atoms are five/six-coordinated CN = 5/6 in the crystal). In Figure 2, we plot the number of

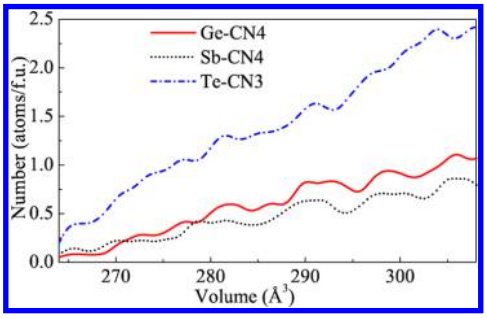

Figure 2. Average number of low-coordinated atoms per formula unit for amorphous structures with an increase in volume. Ge-CN4, Sb-CN4, and Te-CN3 are Ge, Sb, and Te with CNs 4, 4, and 3, respectively.

the most representative low-coordinated atoms, that is, the 3-coordinated Te (Te-CN3), 4-coordinated Sb (Sb-CN4), and 4-coordinated Ge (Ge-CN4), against the volume of the structure. As shown, the low-coordinated atoms for all three elements become more populated with the increase of volume. Among them, the 4-coordinated Ge atom is often in a tetrahedral geometry.[27]

To better understand the bonding pattern in different phases, we have examined the pair distribution functions (PDFs) for Te−Te, Sb−Sb, Ge−Ge, and Ge−Te pairs in four major phases, as shown in Figure 3, each being averaged over all structures of the same phase. Not surprisingly, we found that the heteropolar bond (e.g., Ge−Te bonds) at ~2.9 Å is the dominant first-shell coordination for all phases. Consistently, the homopairs, for example, Te−Te and Sb−Sb, mainly belong

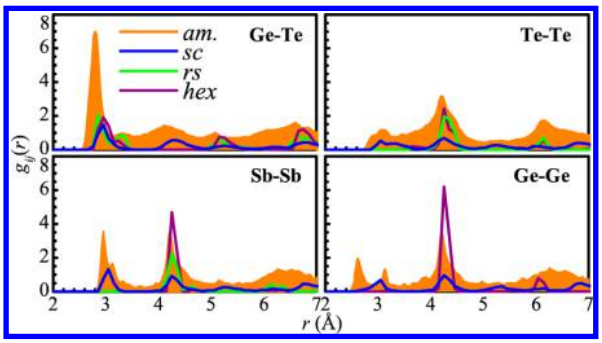

Figure 3. PDFs for Te−Te, Sb−Sb, Ge−Sb, and Ge−Te pairs in four major phases. For clarity, the PDF amplitude of three crystalline phases (***hex***, ***rs***, and ***sc***) is divided by five to compare with that of amorphous structures (***am***).

to the second or third neighbors, exhibiting major peaks at ~4.2 and ~6.5 Å in all phases. This indicates that the amorphous structures retain most of the bonding patterns as the two most stable crystalline phases. On the other hand, new homopolar (Te−Te, Sb−Sb) bonds (the first-shell) evolve at ~2.9 Å in both the amorphous structures and the new ***sc*** phase, indicating the new local bonding patterns. Importantly, while the ***sc*** phase has a similar Ge−Te PDF as those of ***hex***/***rs*** phases, the Te−Te and Sb−Sb PDFs of the ***sc*** phase are in fact much closer to those of the amorphous structures. In particular, the ***sc*** structures exhibit clear homopolar bond peaks at ~2.9 Å, which are not present in ***hex***/***rs*** phases. Therefore, structural analysis of the bonding patterns indicates that the metastable ***sc*** phase acts as a structural bridge to link the amorphous structures with the ***hex***/***rs*** structures.

With all of the structures determined from the global PES, we are now in a position to understand the amorphous-to-crystal transition kinetics. To this end, we utilized the recently developed SSW reaction pathway method to sample the solid-to-solid phase transition pathways between ***rs*** and amorphous structures.[7,17] Specifically, the SSW sampling starts from the ***rs*** crystal structure and visits exhaustively the phases nearby. From 6391 different products connecting to the ***rs*** crystal, we screen out 1200 amorphous structures based on the amorphous criteria established above and utilize the variable-cell double-ended surface walking (VC-DESW) method[19] to locate the transition state (TS) explicitly. Importantly, we find that the amorphous-to-crystal phase transition is generally mediated by metastable intermediates with simple cubic lattice, globally or locally, including the **sc** phase and low-energy amorphous structures. The reaction energy profile and the reaction snapshots for a typical low-energy reaction pathway between ***rs*** and an amorphous structure, ***am-1*** is shown in Figure 4 (other pathways, being similar, are shown in SI Figures S5 and S6).

From Figure 4, we can see clearly that the geometry similarity between ***sc*** and ***rs*** crystals plays a critical role in the low-barrier (0.4 eV/fu) ***rs***-to-***sc*** transition. The ***rs***-to-***sc*** transition is via the collapse of the one-dimensional vacancy row in the ***rs*** crystal, where the Te atoms form homopolar Te−Te bonds in the nascent ***sc*** phase (the Te−Te distance reduces from 4.07 to 3.51 Å) in companion to the formation of Sb−Sb bonds nearby (3.19 Å). This reaction suggests, reversely, that the vacancy creation/annihilation in GST is kinetically facile near homopolar bonds. The low-barrier ***rs***-to-***sc*** transition thus

DOI: 10.1021/acs.jpclett.7b00913
J. Phys. Chem. Lett. 2017, 8, 2560−2564

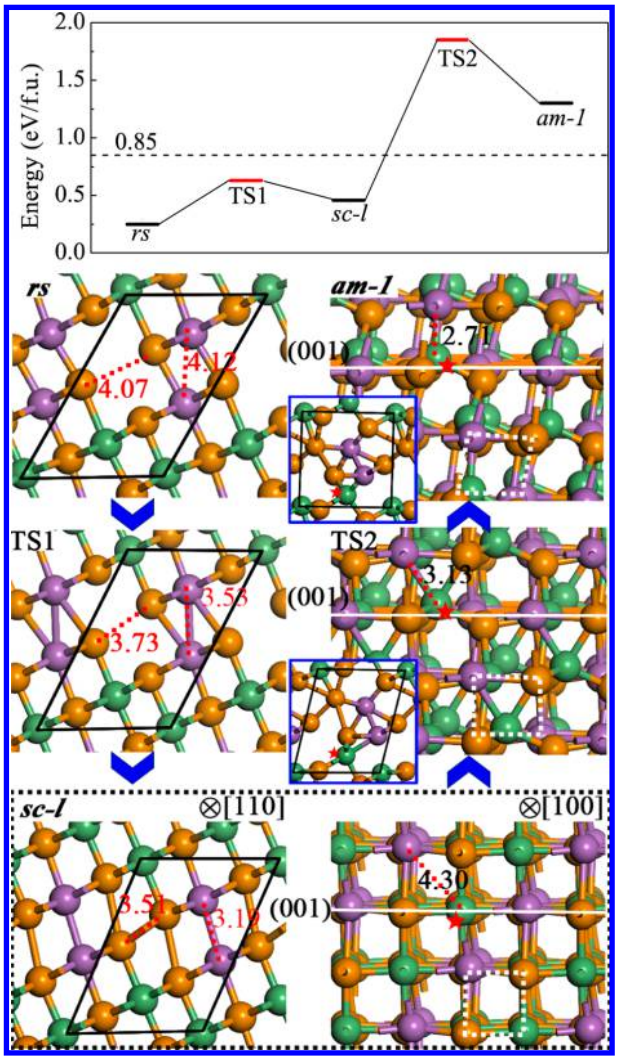

Figure 4. Reaction energy profile and snapshots for a typical *rs*-to-*am* transition identified from SSW pathway sampling. The snapshots are shown in two view angles according to the *sc* lattice: [110] for *rs*-to-*am-1* (those for TS2 and *am-1* shown in the insets) and [100] for *sc*-to-*am-1*.

rationalizes the vacancy formation and the homopolar bond creation in the same theoretical framework.

The next step, the *sc*-to-*am* transition, features the coordination change of Ge (labeled by a star in Figure 4) from octahedron to the tetrahedron coordination. This change is induced initially by the Martensitic shearing of atomic layer (001) along the ⟨120⟩ direction in the *sc* lattice that is accompanied by the local relaxation of atoms. As a result, the as-formed amorphous structure inherits a trace of simple cubic squares, as indicated by the white dotted squares in the reaction snapshots. The final *am-1* structure expands in volume (299 Å^3) due to the formation of low-coordinated Ge and Te atoms.

It should be mentioned that the mechanism of the coordination change of Ge during the *am*-to-*sc* transition observed here differs from the umbrella-flipping model proposed by Kolobov,[2] although the TS at around Ge (TS2 in Figure 4) resembles a flipping umbrella in geometry. From our pathway, it is the Martensitic layer shearing, not the local diffusion of Ge, that drives the change of Ge coordination from the octahedron to tetrahedron. The layer shearing also leads to creation of other homoplar bonds, a key feature of amorphous structures, which is however difficult to explain in the umbrella-flipping model.

Overall, the *am*-to-*rs* transition is kinetically hindered with a barrier no more than 0.6 eV (also see other pathways in the SI). This confirms the kinetics stability of amorphous structures and also the facile transition once the material is heated.[24] Experimentally, the *am*-to-*rs* transition occurs at ∼150 °C, which is lower than that of *am*-to-*hex*, ∼250 °C via the *rs* crystal. From our results, this is simply due to the fact that the subsequent *rs*-to-*hex* transition involves a vacancy diffusion where Ge/Sb atoms move by ∼4 Å. The calculated barrier for the *rs*-to-*hex* transition is 0.9 eV/fu from others' work[23] and 0.8 eV/fu from our DFT results, which is indeed much higher than the barrier of the *am*-to-*rs* transition.

The presence of a metastable *sc* phase in the global PES is of significance for understanding the fast reversible amorphous-to-crystal transition kinetics. Being structurally similar to both *rs* and amorphous structures, it bridges the structural gap in the transition and validates the presence of a local simple cubic lattice in amorphous structures. The inherence of a same simple cubic lattice in all low-energy structures allows fast Martensitic-type shearing of the {100} atomic layer followed by subsequent local relaxation, which is the key to the fast reversible solid transition.

While the presence of the *sc* phase in crystallization might be transient due to the low-barrier transition in *sc*-to-*rs* and the higher stability of the *rs* phase, the simple cubic structure without vacancies was indeed observed previously using MD in the early stage of crystallization,[11,15] and a low concentration of homopolar bonds was left in the as-formed crystals.[1,15] The results here provide new evidence on the key kinetics role of a simple cubic lattice, which supports that the Martensitic layer shearing traditionally regarded for crystal-to-crystal phase transition can also occur in amorphous-to-crystal transition. The methodology utilized in this work is general and thus can facilitate the design of new PCMs via large-scale PES exploration.

■ ASSOCIATED CONTENT

Supporting Information

The Supporting Information is available free of charge on the ACS Publications website at DOI: 10.1021/acs.jpclett.7b00913.

SSW methodology and calculation details; *hex*/*rs* structures; electronic structures for *rs*, *sc-l*, and *am-1* structures; local simple cubic lattice in amorphous structures; other amorphous-to-crystal pathways; and Cartesian coordinates for key states in Figure 4 (PDF)

■ AUTHOR INFORMATION

Corresponding Author

*E-mail: zpliu@fudan.edu.cn.

ORCID

Zhi-Pan Liu: 0000-0002-2906-5217

Li-Min Liu: 0000-0003-3925-5310

Notes

The authors declare no competing financial interest.

■ ACKNOWLEDGMENTS

This work is supported by the National Science Foundation of China (21533001), the Science and Technology Commission

DOI: 10.1021/acs.jpclett.7b00913
J. Phys. Chem. Lett. 2017, 8, 2560−2564

of Shanghai Municipality (08DZ2270500), and the China Postdoctoral Science Foundation (2016M591058).

REFERENCES

(1) Hegedus, J.; Elliott, S. R. Microscopic Origin of the Fast Crystallization Ability of Ge-Sb-Te Phase-Change Memory Materials. *Nat. Mater.* **2008**, *7*, 399−405.
(2) Kolobov, A. V.; Fons, P.; Frenkel, A. I.; Ankudinov, A. L.; Tominaga, J.; Uruga, T. Understanding the Phase-Change Mechanism of Rewritable Optical Media. *Nat. Mater.* **2004**, *3*, 703−708.
(3) Wuttig, M.; Lusebrink, D.; Wamwangi, D.; Welnic, W.; Gillessen, M.; Dronskowski, R. The Role of Vacancies and Local Distortions in the Design of New Phase-Change Materials. *Nat. Mater.* **2007**, *6*, 122−128.
(4) Hosseini, P.; Wright, C. D.; Bhaskaran, H. An Optoelectronic Framework Enabled by Low-Dimensional Phase-Change Films. *Nature* **2014**, *511*, 206−211.
(5) Matsunaga, T.; Akola, J.; Kohara, S.; Honma, T.; Kobayashi, K.; Ikenaga, E.; Jones, R. O.; Yamada, N.; Takata, M.; Kojima, R. From Local Structure to Nanosecond Recrystallization Dynamics in Agnsbte Phase-Change Materials. *Nat. Mater.* **2011**, *10*, 129−134.
(6) Loke, D.; Lee, T. H.; Wang, W. J.; Shi, L. P.; Zhao, R.; Yeo, Y. C.; Chong, T. C.; Elliott, S. R. Breaking the Speed Limits of Phase-Change Memory. *Science* **2012**, *336*, 1566−1569.
(7) Guan, S.-H.; Zhang, X.-J.; Liu, Z.-P. Energy Landscape of Zirconia Phase Transitions. *J. Am. Chem. Soc.* **2015**, *137*, 8010−8013.
(8) Xu, M.; Cheng, Y. Q.; Sheng, H. W.; Ma, E. Nature of Atomic Bonding and Atomic Structure in the Phase-Change $Ge_2Sb_2Te_5$ Glass. *Phys. Rev. Lett.* **2009**, *103*, 195502.
(9) Sen, S.; Edwards, T. G.; Cho, J. Y.; Joo, Y. C. Te-Centric View of the Phase Change Mechanism in Ge-Sb-Te Alloys. *Phys. Rev. Lett.* **2012**, *108*, 195506.
(10) Deringer, V. L.; Dronskowski, R.; Wuttig, M. Microscopic Complexity in Phase-Change Materials and its Role for Applications. *Adv. Funct. Mater.* **2015**, *25*, 6343−6359.
(11) Lee, T. H.; Elliott, S. R. Structural Role of Vacancies in the Phase Transition of $Ge_2Sb_2Te_5$ Memory Materials. *Phys. Rev. B: Condens. Matter Mater. Phys.* **2011**, *84*, 094124.
(12) Ronneberger, I.; Zhang, W.; Eshet, H.; Mazzarello, R. Crystallization Properties of the $Ge_2Sb_2Te_5$ Phase-Change Compound from Advanced Simulations. *Adv. Funct. Mater.* **2015**, *25*, 6407−6413.
(13) Ohara, K.; Temleitner, L.; Sugimoto, K.; Kohara, S.; Matsunaga, T.; Pusztai, L.; Itou, M.; Ohsumi, H.; Kojima, R.; Yamada, N.; et al. The Roles of the Ge-Te Core Network and the Sb-Te Pseudo Network During Rapid Nucleation-Dominated Crystallization of Amorphous $Ge_2Sb_2Te_5$. *Adv. Funct. Mater.* **2012**, *22*, 2251−2257.
(14) Lee, T. H.; Elliott, S. R. Ab Initio Computer Simulation of the Early Stages of Crystallization: Application to $Ge_2Sb_2Te_5$ Phase-Change Materials. *Phys. Rev. Lett.* **2011**, *107*, 145702.
(15) Kalikka, J.; Akola, J.; Larrucea, J.; Jones, R. O. Nucleus-Driven Crystallization of Amorphous $Ge_2Sb_2Te_5$: A Density Functional Study. *Phys. Rev. B: Condens. Matter Mater. Phys.* **2012**, *86*, 144113.
(16) Zhu, S.-C.; Xie, S.-H.; Liu, Z.-P. Nature of Rutile Nuclei in Anatase-to-Rutile Phase Transition. *J. Am. Chem. Soc.* **2015**, *137*, 11532−11539.
(17) Li, Y.-F.; Zhu, S.-C.; Liu, Z.-P. Reaction Network of Layer-to-Tunnel Transition of MnO_2. *J. Am. Chem. Soc.* **2016**, *138*, 5371−5379.
(18) Shang, C.; Zhang, X.-J.; Liu, Z.-P. Stochastic Surface Walking Method for Crystal Structure and Phase Transition Pathway Prediction. *Phys. Chem. Chem. Phys.* **2014**, *16*, 17845−17856.
(19) Zhang, X.-J.; Liu, Z.-P. Variable-Cell Double-Ended Surface Walking Method for Fast Transition State Location of Solid Phase Transitions. *J. Chem. Theory Comput.* **2015**, *11*, 4885−4894.
(20) Shang, C.; Liu, Z.-P. Stochastic Surface Walking Method for Structure Prediction and Pathway Searching. *J. Chem. Theory Comput.* **2013**, *9*, 1838−1845.
(21) Zhu, S.-C.; Xie, S.-H.; Liu, Z.-P. Design and Observation of Biphase TiO_2 Crystal with Perfect Junction. *J. Phys. Chem. Lett.* **2014**, *5*, 3162−3168.
(22) Steinhardt, P. J.; Nelson, D. R.; Ronchetti, M. Bond-Orientational Order in Liquids and Glasses. *Phys. Rev. B: Condens. Matter Mater. Phys.* **1983**, *28*, 784−805.
(23) Zhang, B.; Zhang, W.; Shen, Z.; Chen, Y.; Li, J.; Zhang, S.; Zhang, Z.; Wuttig, M.; Mazzarello, R.; Ma, E.; et al. Element-Resolved Atomic Structure Imaging of Rocksalt $Ge_2Sb_2Te_5$ Phase-Change Material. *Appl. Phys. Lett.* **2016**, *108*, 191902.
(24) Siegrist, T.; Jost, P.; Volker, H.; Woda, M.; Merkelbach, P.; Schlockermann, C.; Wuttig, M. Disorder-Induced Localization in Crystalline Phase-Change Materials. *Nat. Mater.* **2011**, *10*, 202−208.
(25) Krbal, M.; Kolobov, A. V.; Haines, J.; Fons, P.; Levelut, C.; Le Parc, R.; Hanfland, M.; Tominaga, J.; Pradel, A.; Ribes, M. Initial Structure Memory of Pressure-Induced Changes in the Phase-Change Memory Alloy $Ge_2Sb_2Te_5$. *Phys. Rev. Lett.* **2009**, *103*, 115502.
(26) Chekmarev, D. S.; Oxtoby, D. W.; Rice, S. A. Melting of a Quasi-Two-Dimensional Metallic System. *Phys. Rev. E: Stat. Phys., Plasmas, Fluids, Relat. Interdiscip. Top.* **2001**, *63*, 051502.
(27) Mazzarello, R.; Caravati, S.; Angioletti-Uberti, S.; Bernasconi, M.; Parrinello, M. Signature of Tetrahedral Ge in the Raman Spectrum of Amorphous Phase-Change Materials. *Phys. Rev. Lett.* **2010**, *104*, 085503.

DOI: 10.1021/acs.jpclett.7b00913
J. Phys. Chem. Lett. 2017, 8, 2560−2564